The International Journal of Advanced Manufacturing Technology (2022) 121:4885–4904
https://doi.org/10.1007/s00170-022-09673-4

ORIGINAL ARTICLE

Experimental and numerical investigation into material removal mechanism of fast ED-milling

Jian Wang[1,2] · Xue-Cheng Xi[1,2] · Hao-Yu Chu[1,2] · Ya-Ou Zhang[1,2] · Fu-Chun Zhao[2] · Wan-Sheng Zhao[1,2]

Received: 10 May 2022 / Accepted: 3 July 2022 / Published online: 12 July 2022

Abstract
Fast electrical discharge milling (fast ED-milling) has become a promising technology in the manufacturing industry for machining complex structures such as diffuser-shaped film cooling holes. However, the mechanism of the efficient removal of materials in this technology is not yet fully understood. To gain a further insight into this matter, an experimental investigation on the morphology of discharge craters including the absolute material removal volume per discharge, material residual volume per discharge, and directionality, is firstly carried out. The obtained results imply that a high-pressure inner flushing can significantly promote the expelling of molten material from a molten pool and is a fundamental reason why fast ED-milling can be of higher machining efficiency than regular ED-milling. To explore the mechanism behind, a novel thermal-fluid coupling model is developed to simulate the evolution process of the molten material under the effect of a flow field. The results of numerical simulation show that during a discharging, the molten material moves along the workpiece surface towards the outlet of a gap channel and solidifies at the side of a crater that is away from the electrode center. Another interesting finding is that an inappropriately high flushing pressure can result in a low machining efficiency because the severe heat convection will consume a large part of the heat generated by a discharge. This well explains the phenomenon that occurred during the experimental investigation.

Keywords Fast electrical discharge milling · Material removal mechanism · Flushing condition · Molten material · Thermal-fluid coupling model · Numerical simulation

1 Introduction

Electrical discharge machining (EDM) milling is a widely utilized manufacturing process in aviation and biomedical industries for machining cavities and complex structures in difficult-to-cut materials [1]. This technology removes materials from a workpiece in a layer-by-layer manner by using a simple-shaped tool electrode that moves along a predetermined tool path while rotating. In conventional ED-milling, petrolic dielectric and immersed flushing are applied as dielectric and flushing conditions, respectively. Although it has been proved that this processing technology can achieve a satisfactory machining accuracy [2, 3], however, it suffers from low machining efficiency severely, which impedes an extensive application of EDM milling in mass production.

Conversely, fast ED-milling, which applies deionized water as dielectric, a brass tubular as a tool electrode, and high-pressure inner flushing as flushing condition, has become a promising technology in the aerospace industry due to its high machining efficiency and easy implementation [4, 5]. Having a machining condition similar to that of fast ED-drilling, this technology can be integrated into an existing multi-axis ED-drilling machine. This is particularly important when machining diffuser-shaped film cooling holes. In this case, diffusers can be milled on the same fast ED-drilling machine where cylindrical holes are drilled, thus the alignment errors caused by secondary clamping and the low machining efficiency resulting from frequent electrode redressing in the sinking EDM of diffusers can be avoided.

However, up to now, studies on fast ED-milling mainly remain in feasibility verification and industrial application [6, 7], the material removal mechanism, by which fast ED-milling is more efficient in material removal than regular

✉ Xue-Cheng Xi
xixuecheng@gmail.com

[1] State Key Laboratory of Mechanical System and Vibration, Shanghai 200240, China

[2] School of Mechanical Engineering, Shanghai Jiao Tong University, Shanghai 200240, China

ED-milling, is yet to be clarified. The existing explanation for this phenomenon is usually macroscopic and empirical, that is, similar to fast ED-drilling [8], the use of high-pressure inner flushing improves the evacuation efficiency of debris dramatically. Nevertheless, this explanation is partial since the efficient evacuation of debris only improves the machining stability, and is not the root cause of a high material removal rate. Inspired by the works reported in [9, 10], an in-depth investigation on the influence of a flow field on a discharge process itself, such as the movement of molten material, may fundamentally reveal the reasons for the effective removal of materials.

To investigate the effect of a flow field on a discharge process, direct observations of the discharge gap with a high-speed camera are of great help. By using a high-speed camera and a thermal-fluid coupling model, Chu et al. [10] studied the formation and movement of the molten material in fast ED-drilling, it has been found that the moving direction of the molten material was consistent with that of a high-speed flushing fluid. Similarly, Zhu et al. [11] investigated the arc plasma expansion and deflection behavior in air flushing electrical arc machining, and found a similar phenomenon. With air as dielectric, Yue et al. [12] used a high-speed camera to monitor the material removal and molten pool movement in conventional EDM. The observation results showed that the spattering direction of the removed molten materials from a workpiece was approximately along with the direction of a flow field. The above-mentioned studies confirmed that a flow field plays a crucial role in the movement of molten metal and verified the feasibility of using a high-speed camera to observe a discharge process directly. However, due to the severe flushing fluid splashing, opaque workpiece, and debris spattering in fast ED-milling, it is difficult for a high-speed camera to focus on the discharge spot and records an entire discharge process.

In addition to direct observation, static analysis of discharge crater combined with process numerical simulation is another powerful method to uncover the driving forces of the trend of the molten material movement. Zhu et al. [11] studied the morphology of craters generated by single-pulse discharges under various air flushing velocities and the results showed that with an effective air flushing, the molten metal is more effectively expelled from a molten pool and seldom recasts near the crater, which indicates that air flushing can improve the material removal efficiency. Zhang et al. [13] studied the high-pressure flushing effect in blasting erosion arc machining (BEAM) by applying the computational fluid dynamic (CFD) method. Their results indicated that high-speed water flushing can form a low-pressure area on the downstream side of an electrode, which can expel the molten metal into the surrounding dielectric and enhance the material removal rate significantly. Although the mentioned researches are not for the fast ED-milling itself, their methodology, i.e., using a combination of single-pulse discharge experiment and numerical simulation to investigate the effect of a dielectric flow field on a discharge process, is still of great reference significance for this work.

Based on the above discussion, this paper attempts to discover the mechanism behind the efficient material removal by analyzing the influence of a dielectric flow field on the movement of molten material. A multi-pulse discharge experiment that considers the characteristics of an applied pulse generator is firstly conducted to investigate the geometric morphology of discharge craters including the absolute material removal volume per discharge, the residual volume per discharge, and directionality. By comparing the geometric morphology of craters that are generated under various dielectric and flushing conditions, the reason why fast ED-milling has a conspicuous promotion in the material removal rate over conventional ED-milling can be uncovered. To explore the mechanism behind and explain the phenomena that occurred during experiments, a novel thermal-fluid coupling model which considers high-speed inner flushing and special geometric properties is developed.

2 Multi-pulse discharge experiment

2.1 Experimental setup

Single-pulse discharge experiment is widely adopted while investigating the discharge phenomenon in other EDM processes [14, 15]. However, as per the nature of fast ED-milling, a resistance–capacitance (RC) pulse generator is usually applied in real machining rather than a transistorized pulse generator to obtain a higher machining efficiency. In this case, it can hardly ensure that there is only one discharge occurring during each experiment. Similarly, there is no guarantee that a crater on a workpiece is generated only by a single discharge. In fact, it is often found in actual machining that once the dielectric is broken down, trains of discharges will sequentially take place, as described in Fig. 1. This is undesirable to researches on geometric parameters such as dimension and residual stress of craters [16, 17]. Fortunately, this study focuses on the material removal and residual volume per discharge, as well as the moving tendency of molten material in fast ED-milling, if the number of discharges occurring during an experiment can be accurately counted, these evaluation indicators can be obtained more meaningfully. Besides, to ensure that the obtained results can be used as a guide for the actual machining, the experimental conditions should be set up as close as possible to the physical condition of this specific machining process. Therefore, this paper is not limited to considering a single-pulse discharge crater, but studies the statistical role of crater morphology under the action of multiple discharges. Moreover, the influence of random errors can be eliminated to a certain extent by averaging

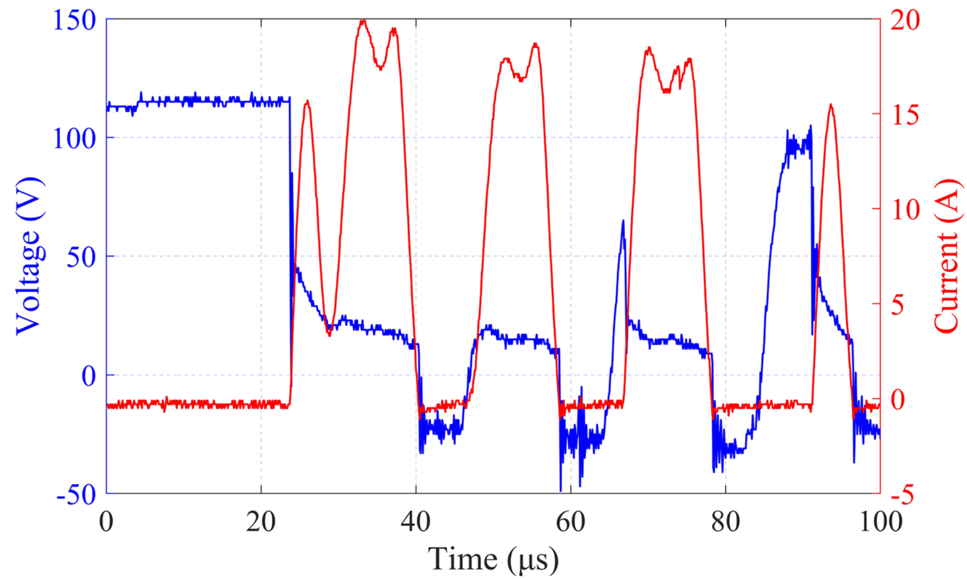

Fig. 1 Sequential discharges occurred during an experiment

the measured volume of craters generated by a series of discharges. The movement tendency of molten material under the effect of a flow field can also be observed more obviously as well.

Based on the above discussion, a multi-pulse discharge experimental method considering the characteristics of actual processing conditions and the evaluation indicators was developed. The experiments were conducted on the ZGCNC-6, a six-axis fast ED-drilling machine equipped with additional milling functionality, as shown in Fig. 2. Benefiting from applying the Panasonic EtherCAT AC servo drivers, a homemade high-performance CNC controller for this machine offers highly dynamic and compact servo control hardware, enabling real-time servo control with a cycle of 1 ms for machining processes. During the experiment, the number of discharges and the geometrical morphology of a crater are measured to analyze the effect of dielectric flushing on the movement of molten material, which will be further introduced in Sect. 2.2. The schematic diagram of the multi-pulse discharge experimental setup is illustrated in Fig. 3. As can be seen from the figure, an RC pulse generator is utilized to supply the discharge energy. A brass tube with a nominal outer diameter of 0.6 mm, an inner diameter of 0.2 mm, and a length of 400 mm is used as the tool electrode. The workpiece material is a nickel-based superalloy and its composition is listed in Table 1. The default machining parameters used in these machining tests are listed in Table 2, unless specified otherwise.

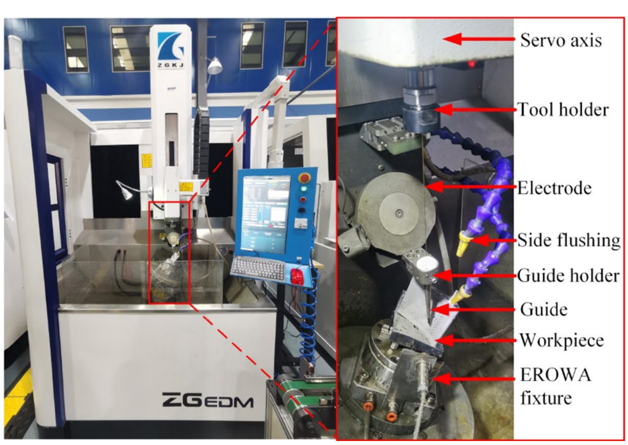

Fig. 2 The fast ED-drilling and milling machine

A Tektronix® THDP0100 high voltage differential probe, and a Tektronix® TCP303 current probe accompanied with a Tektronix® TCPA300 amplifier are used to measure the gap voltage and current, respectively. Measured signals are analyzed by an SDS2204X Plus digital oscilloscope for pulse counting and triggering. Before ignition of the discharge, the CNC system controls the electrode to feed down slowly from an initial position that is far larger than the discharge gap via the EtherCAT protocol. At the same time, the TCP/IP protocol is used by the CNC system to continuously interact with the oscilloscope in a 1 ms cycle to monitor whether the oscilloscope is triggered by the breakdown or not. Once the oscilloscope is triggered by the discharge current signal, the CNC system will acquire the trigger signal within a delay of up to 1 ms, and then raise the electrode to the initial position within 2 ms to terminate the discharge. This strategy guarantees that the overall delay from the initial occurrence of a discharge to the end of the experiment does not exceed 4 ms. To accurately obtain the number of discharges occurring during each experiment, the time base of the oscilloscope is firstly set to 2 ms to record gap signals within 10 ms from triggering, and then the time base was reduced to 50 μs to count the number of discharges, as shown in Fig. 4.

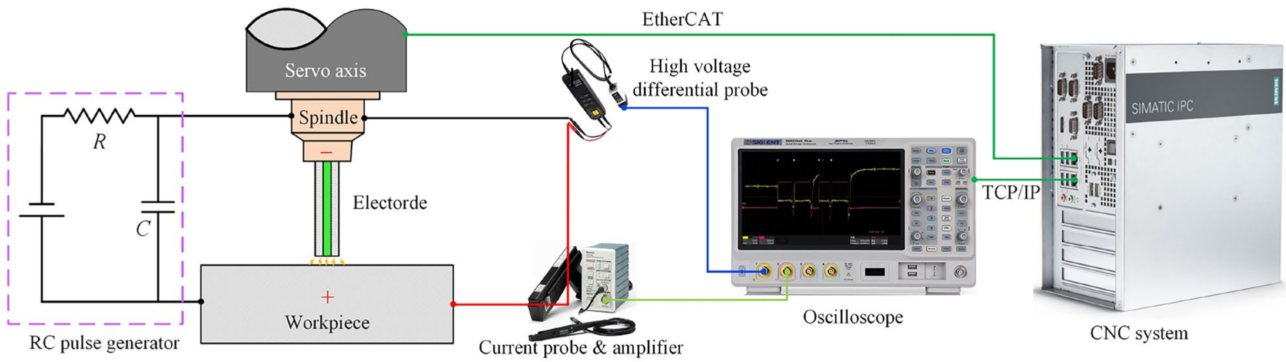

Fig. 3 Schematic diagram of the multi-pulse discharge experimental setup

2.2 Definition of combined crater morphology

To numerically denote the results of the multi-discharge experiments, an Alicona InfiniteFocus G5 optical three-dimensional measurement system is applied to measure the cross-section profiles and the volume of a discharge crater. The measured results of a typical crater are shown in Fig. 5. It can be seen that with two discharges, an irregular crater is formed on the surface of a workpiece, with bulges formed around its edges. This is because instantaneous high-temperature discharges melt the workpiece material resulting in a molten pool, a part of the molten material in the molten pool is dispelled into the gap to be completely removed, the remaining molten material solidifies and adhesives along a crater to form a recast layer and surrounded bugles, respectively. Since the combined craters in the experiments are not necessarily generated by a single discharge, the depth and area of the combined craters are not discussed. In this paper, the focus is the absolute material removal volume per discharge V_r, the material residual volume per discharge V_ε, and the directionality of the crater. V_r and V_ε can be calculated by

$$V_r = \frac{V_{below} - V_{above}}{N} \tag{1}$$

$$V_\varepsilon = \frac{V_{above}}{N} \tag{2}$$

where V_{above} stands for the volume of the re-solidified material above the workpiece surface, V_{below} represents the volume of the crater below the workpiece surface, N denotes the number of discharges occurring during the test, as illustrated in Fig. 5b. From the definition of V_r and V_ε, it can be concluded that V_r can be used to represent the material removal rate and the scouring ability of an applied flushing condition for molten material, V_ε stands for the surface quality of the machined surface.

The directionality of a combined crater refers to the moving trend of the molten material under the effect of a flushing flow field, which can be evaluated by the height of bulges. Specifically, a larger bulge height means an accumulation of re-solidified material, indicating that the molten material tends to move toward this position under the action of the flow field. To this end, as shown in Fig. 5c, the cross-section profiles are measured in two different directions to obtain the bugle heights at different positions, so that the movement direction of molten materials can be characterized.

Table 1 Composition of the applied nickel-based superalloy

Elements	Ni	Cr	Fe	Nb	Al	Ti
Weight (%)	54.48	17.50	22.3	4.90	0.66	0.96

3 Mechanism investigation

As mentioned above, the objective of this paper is to reveal the fundamental reason why the fast ED-milling is of higher material removal rate than conventional ED-milling. In terms of machining conditions, there are two significant differences between them, i.e., the dielectric fluids and their flushing conditions. Being different from conventional ED-milling which uses immersed flushing and petrolic dielectric, fast ED-milling applies high-pressure inner flushing of deionized water to evacuate the debris and cool a gap. Therefore, in this section, the influence of dielectric and flushing conditions on the geometric morphology of combined craters are investigated.

Table 2 Default machining parameters

Parameter	Value
Pulse duration (μs)	10
Pulse interval (μs)	10
Peak current (A)	12.5
Capacitance (μF)	0.377
Spindle speed (rpm)	300
Polarity (tool electrode)	Negative

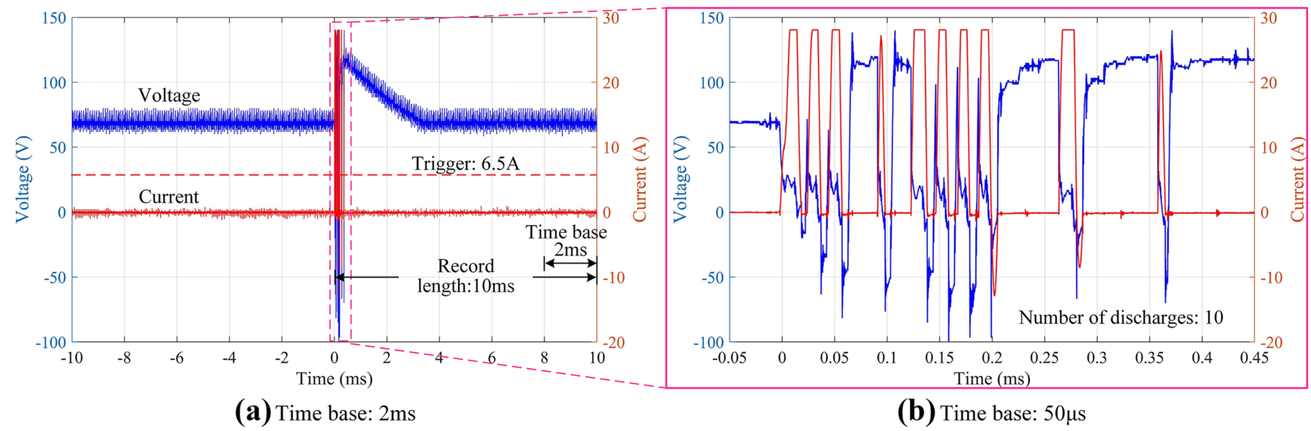

Fig. 4 Voltage and current waveforms acquired by the oscilloscope (redrawn by MATLAB R2020a)

3.1 Influence of dielectric fluids

To accurately compare the effect of dielectric on the geometric morphology of discharge craters, a comparative experiment is conducted on the developed experimental setup. By using the machining parameters listed in Table 2, EDM-oil and deionized water are used, respectively, as a dielectric to conduct the multi-pulse discharge experiments under immersed flushing, as shown in Fig. 6. For each dielectric, 20 repeated experiments are carried out and the obtained results are averaged as the final results, as illustrated in Fig. 7. From the figure, it can be observed that when deionized water is used as the dielectric, V_r is much smaller than that when EDM-oil is used. It can thus be concluded that the use of deionized water is not the reason why the machining efficiency of fast ED-milling is higher than

Fig. 5 Measurement results of geometrical morphology of a combined discharge crater

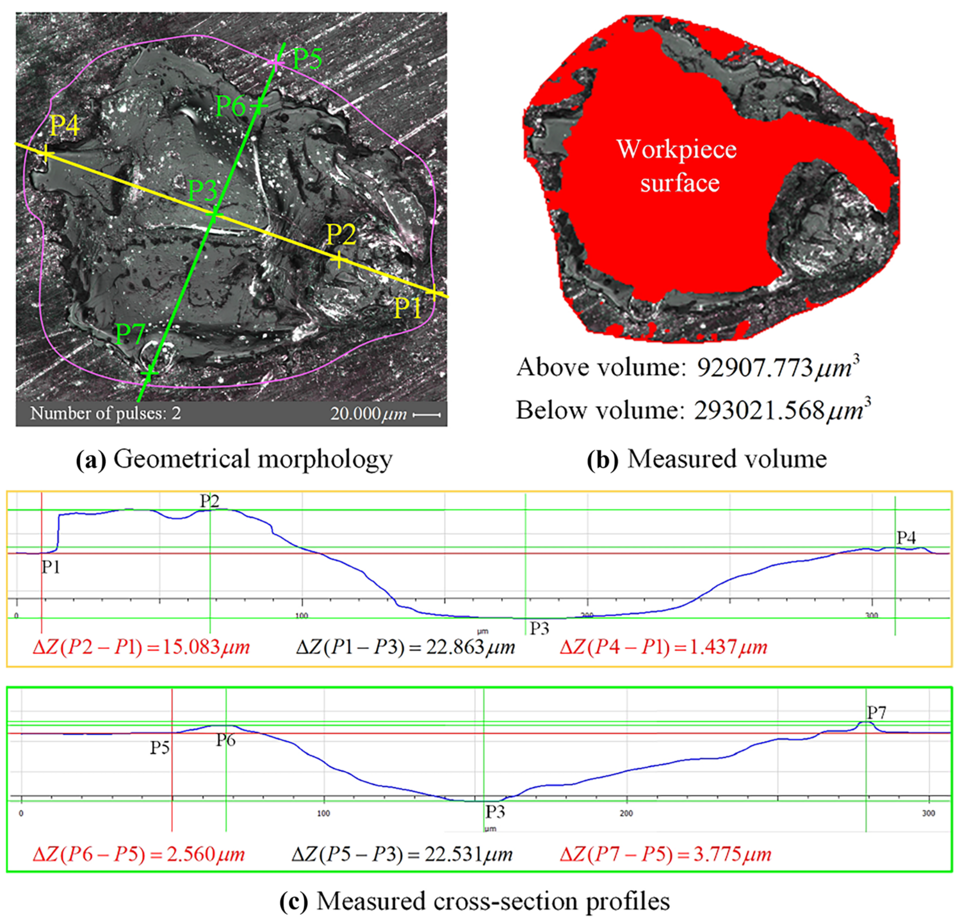

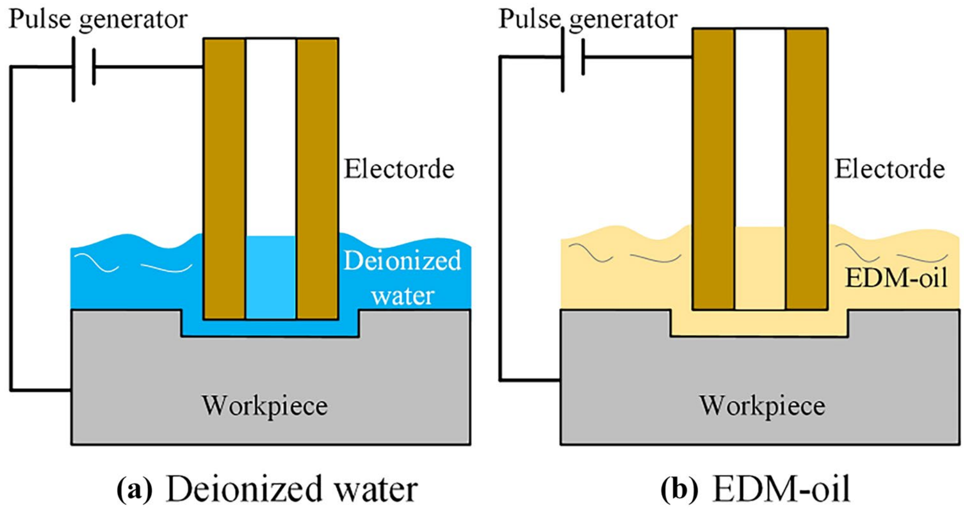

Fig. 6 Flushing condition for investigating the effect of dielectric fluids

that of conventional ED-milling. Moreover, the comparison results of V_ε show that with the use of deionized water, better surface roughness can be obtained.

To compare the effect of dielectric on crater directionality, experiments with the highest V_r are used to visualize the geometric morphology, as shown in Figs. 8 and 9. From Fig. 8, it can be observed that although the conductivity of deionized water used is sufficiently small (about 0.8 μS/cm), serious stray current corrosions still occur during machining. The workpiece surface is drastically etched and pitted, resulting in a poor surface quality. By contrast, when EDM-oil is used as the dielectric fluid, the workpiece surface finds no evidence of electrochemical erosion, as can be seen from Fig. 9. In terms of the crater directionality, it can be found in Fig. 8 that bulges are mainly distributed along the radial direction of the electrode. This can be explained by the fact that the solid material of the electrode at the circumferential direction constrains the expansion of a discharge plasma channel, while the discharge plasma channel can only expand freely along the radial direction since the existence of the inner channel and the outer dielectric. As illustrated in Fig. 9, the height of the bulges near the external surface of the electrode is significantly lower than that near the internal surface, which means that the molten material has accumulated near the internal surface of the electrode during machining. This is because the amount of dielectric in the internal channel is too small to cool the generated molten material sufficiently.

3.2 Influence of flushing conditions

Experiments conducted in Sect. 3.1 verify that the use of deionized water is not the dominant factor for relevant higher material removal rate obtained by fast ED-milling as compared to conventional ED-milling. Now the problem is to investigate the effect of flushing conditions. Therefore, in this section, based on the multi-pulse discharge experiments, influences of some commonly applied flushing conditions

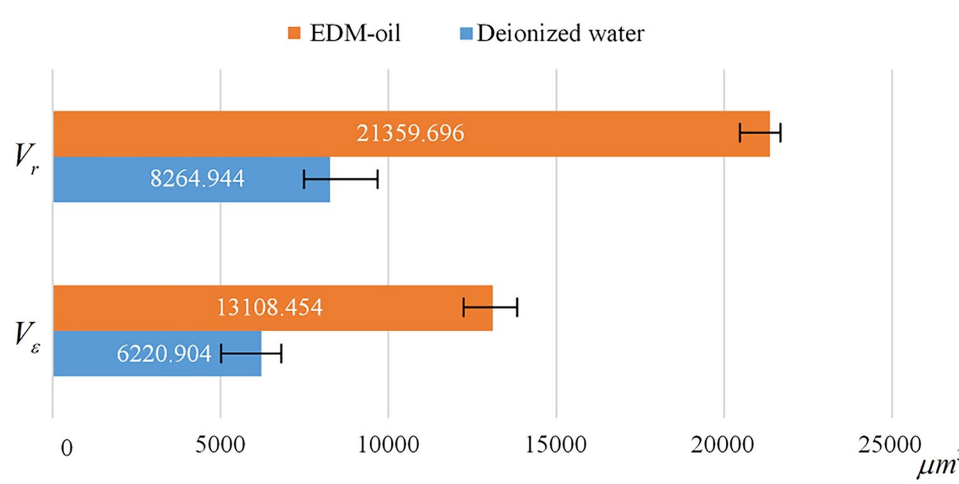

Fig. 7 Experimental results of the effect of dielectric fluids on crater geometric morphology

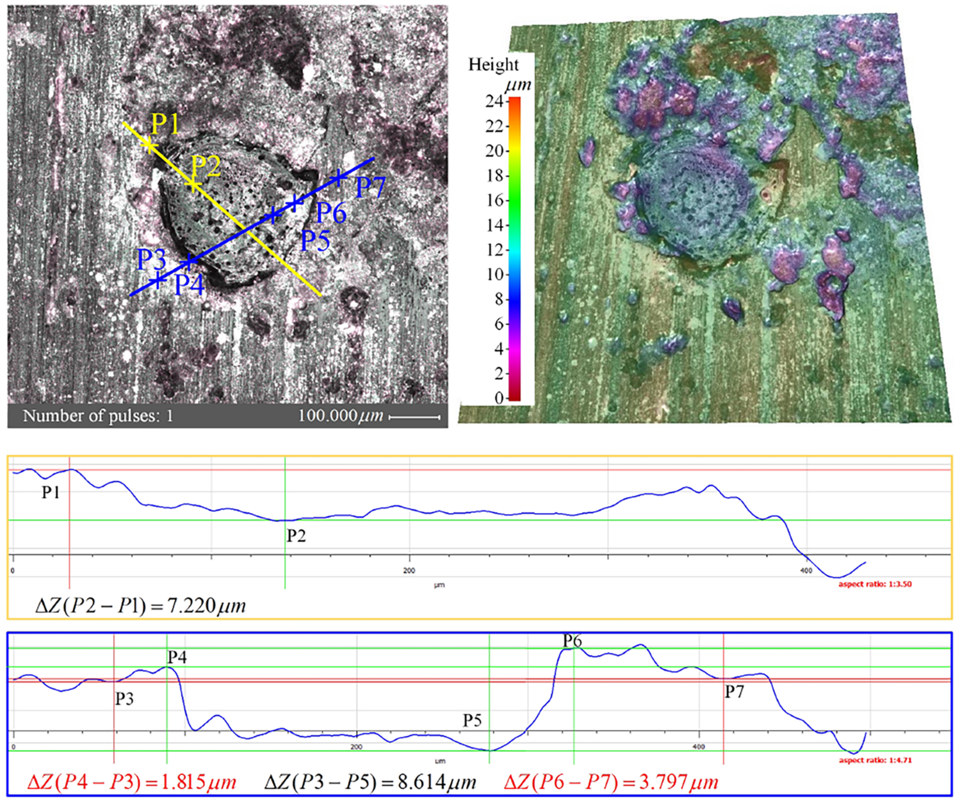

Fig. 8 Geometrical morphology of a combined crater with deionized water as the dielectric fluid

on crater morphology are compared. The flushing conditions considered in the experiments are shown in Fig. 10. In addition to the machining parameters listed in Table 2, an internal and side flushing with constant flushing pressures of 0.48 and 0.2 MPa are also applied. The experimental results refer to the average V_r and V_ε with twenty repetitions of the experiments per each flushing condition are shown in Fig. 11.

From Fig. 11 it can be seen that compared with immersed flushing, by using side flushing, V_ε can be reduced while V_r can be improved. This means that a moving flow field has a positive influence on a discharge process. Moreover, compared with immersed flushing with EDM-oil, with high-pressure inner flushing of deionized water, V_r and V_ε are greatly increased by 29.6% from 21,359.696 to 30,351.565 μm^3, and 7.4% from 13,108.454 to 14,079.299 μm^3, respectively. The increase of V_r indicates that the high-pressure inner flushing facilitates the molten material to be expelled from a molten pool during machining. The increase of V_ε can be explained by the fact that under a specified flushing condition, the proportion of the completely removed molten material volume to the total expelled molten material from a molten pool is constant, hence, an increase of the total amount of the expelled molten material increases the amount of the molten material that is solidified on the workpiece surface. Besides, V_r is increased by 13.3% from 30,351.565 to 31,574.800 μm^3 while V_ε is reduced by 22.8% from 14,079.299 to 10,858.707 μm^3 when a combination of side and inner flushing is applied. The increase of V_r and the decrease of V_ε indicate that the side flushing can enhance the cooling ability of the dielectric and promote the removal of molten metal. Figure 11 also shows that a combination of immersed and inner flushing can improve V_r to a certain extent, but has no noticeable effect on V_ε. Therefore, based on the experimental results, the following conclusions can be drawn. Firstly, the use of high-pressure inner flushing is the predominant factor that determines why fast ED-milling offers much higher machining efficiency than regular ED-milling. Secondly, a combination of side and inner flushing is a better flushing arrangement for fast ED-milling. Thirdly, compared with conventional ED-milling, with side and inner flushing, a higher material removal rate and a better surface quality can be achieved with fast ED-milling.

To investigate the effect of flushing conditions on the directionality of craters, in the same vein, experiments with the highest V_r are used to visualize the geometric morphology, as shown in Fig. 12 through Fig. 15. As illustrated in Fig. 12, the bugle heights of craters increase significantly along the side flushing direction, indicating that the molten material moves along the flushing direction under the effect of a flow field induced by side flushing. Another noticeable phenomenon is that with an inner flushing of deionized

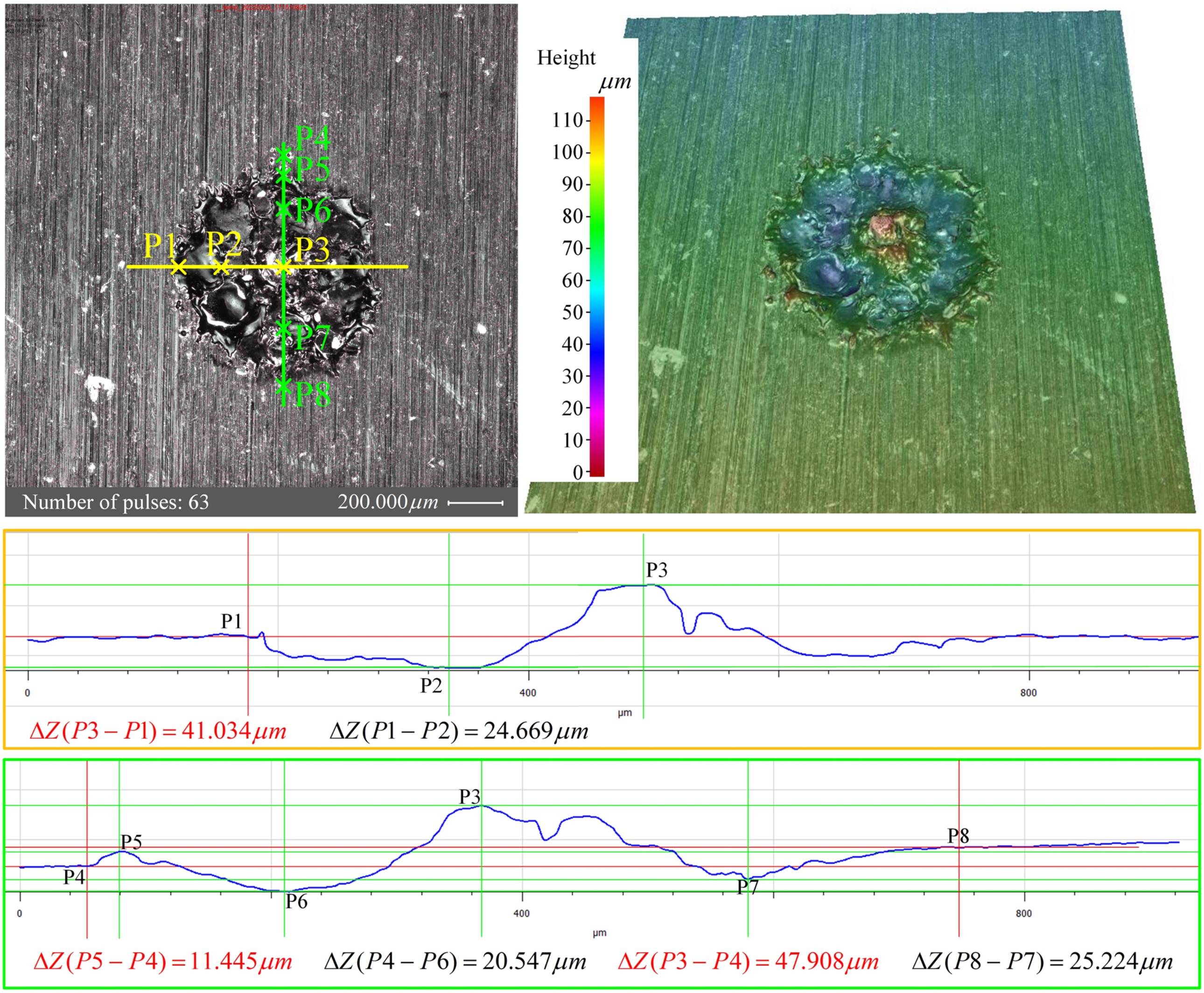

Fig. 9 Geometrical morphology of a combined crater with EDM-oil as the dielectric fluid

water, the distribution of bulge heights around the crater obviously shows an opposite trend with that of the case in which immersed flushing with EDM-oil is applied, as depicted in Fig. 13 through Fig. 15. The height of the bulges near the external surface of the electrode is significantly larger than that near the internal surface (Fig. 14). This shows that under the effect of a high-pressure internal flow field, the molten material tends to move towards the external surface of the electrode during machining. As for the surface quality, as shown in Figs. 12 and 15, stray current corrosions still occur when side flushing or immersed combined with inner flushing is used. The difference is that the formed corrosion pits are much smaller and more densely distributed on the machined surface. This indicates that side flushing and immersed combined with inner flushing are not suitable for fast ED-milling.

3.3 Influence of flushing pressure

This section is aimed to analyze the influences of inner flushing pressure P_{in} on V_r and V_ε. Similarly, based on the multi-pulse discharge experiments, by using a combination of side and inner flushing, V_r and V_ε of craters generated on a workpiece surface under various inner flushing pressures are compared. The comparative experiments are repeated twenty times and the average values of V_r and V_ε are considered as the final result, as shown in Fig. 16.

What is striking in Fig. 16 is that as the inner flushing pressure P_{in} increases, the average absolute material removal volume per discharge V_r increases rapidly at first and peaks at 45,171.83 μm^3 when P_{in} is 0.69 MPa, then shows a decreasing trend. This is because an appropriate increase in P_{in} can promote the evacuation of molten material from a molten

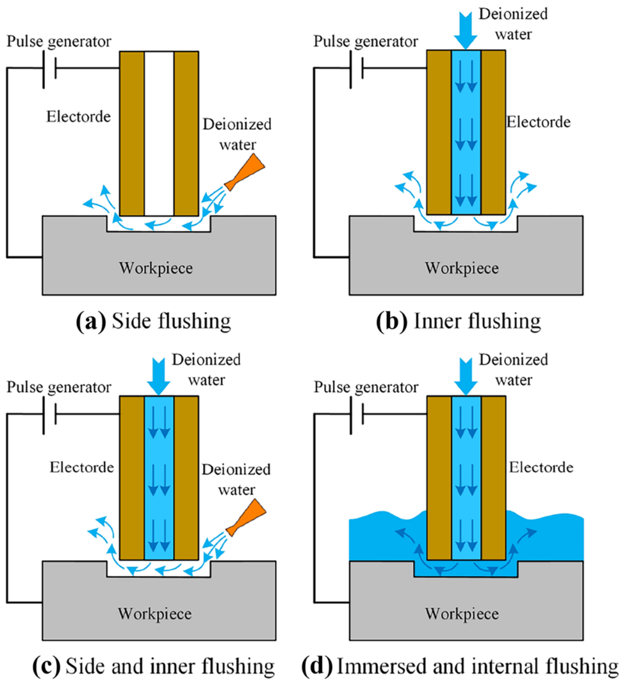

Fig. 10 Flushing conditions compared in the experiments

pool, thus the material removal volume can be increased. A possible explanation for the unexpected decline is that as the flushing pressure increases, the velocity of the flushing fluid near the discharge position increases as well. Due to the heat convection, the heat taken away by the high-speed flushing dielectric accounts for an increasing proportion of the total heat generated by discharges, so that the remaining heat is insufficient to generate molten material, resulting in a decrease in V_r. Moreover, a significant reduction in V_ε is found when P_{in} increases from 0.21 Mpa to 0.48 MPa. With a further increase in P_{in}, V_ε remains relatively steady until P_{in} exceeds 0.69 MPa. This is due to the fact that under the effect of a high-speed flushing fluid, the molten material can be efficiently washed away, resulting in less molten material solidifying on the workpiece surface. The remarkable decline in V_ε with a large P_{in} resulted from the reduced total molten material generated in the molten pool.

4 Thermal-fluid coupling model for fast ED-milling

In Sect. 3, the promotion influence of a flow field induced by high-pressure inner flushing on a fast ED-milling process is proven by the analysis of crater morphology. However, the dynamic evolution process of molten material in the combined crater under the effect of a fluid field remains unclear. Without this, it is impossible to explain the directionality of the combined craters and the variation trend of V_r with respect to P_{in}. Therefore, on the platform of COMSOL Multiphysics 6.0, a novel thermal-fluid coupling model, which incorporates a high-pressure inner flushing and the special geometric properties, is developed. This thermal-fluid model is used to investigate a complete process of generation, movement, and solidification of molten material generated by a single discharge in a multi-pulse discharge experiment. A conjugate heat transfer module, a turbulent two-phase flow module, a phase change module, and a level-set method are combined to simulate an evolution process of molten material. Based on the temperature, velocity, and pressure fields from the model, the moving tendency of molten material and the phenomenon occurring during the abovementioned experiments can be explained. The details of the model are illustrated as follows.

Fig. 11 Effects of flushing condition on crater geometric morphology

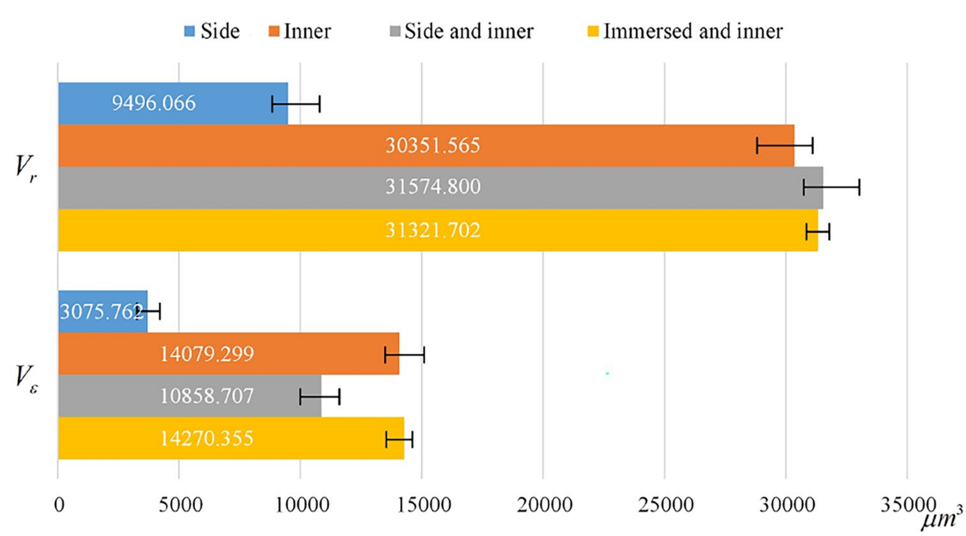

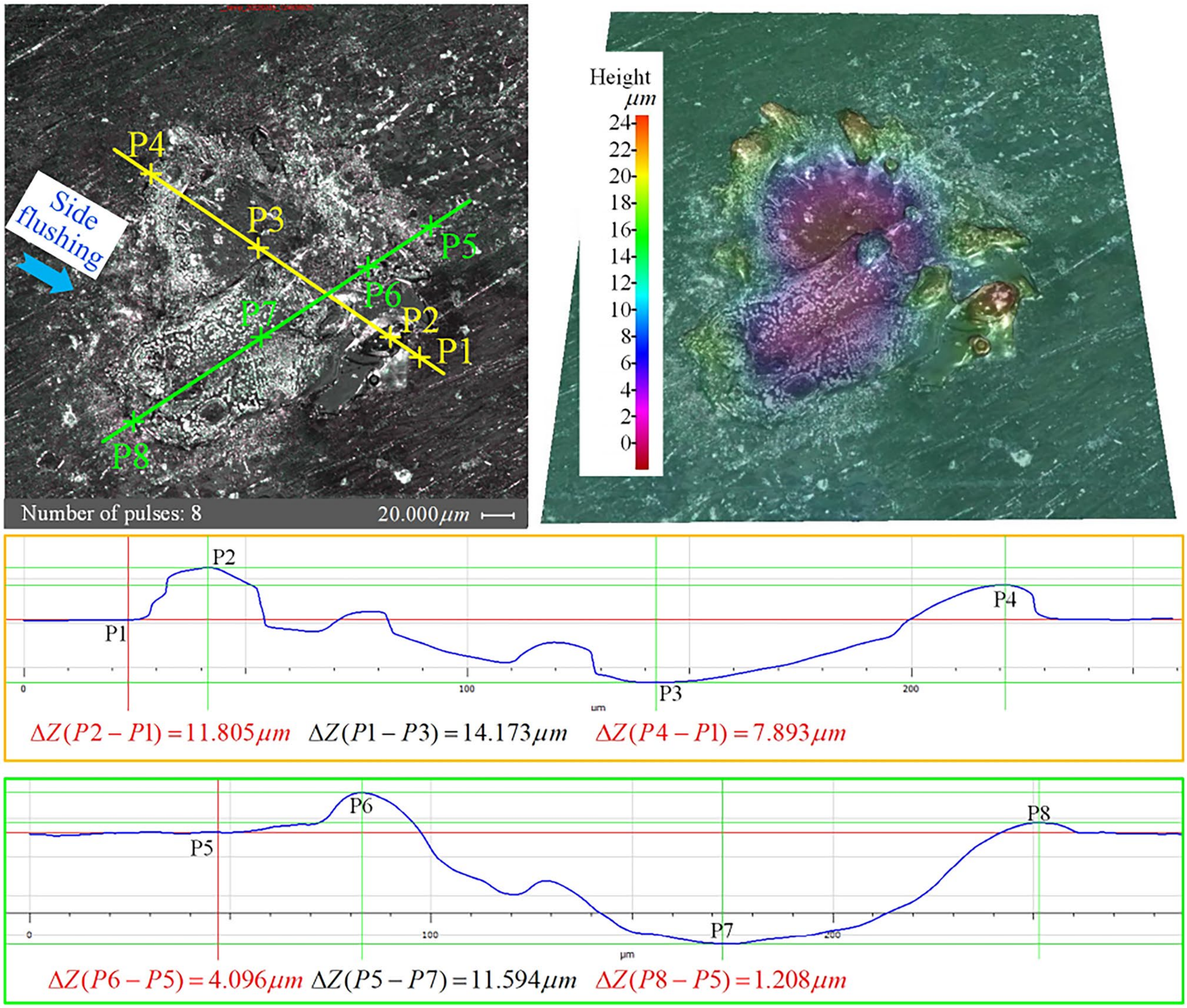

Fig. 12 Geometrical morphology of a combined crater when side flushing is applied

4.1 Assumptions

To establish the coupling model, some reasonable assumptions and declarations are needed to be made first to simplify the calculation.

1. The workpiece material is homogeneous and isotropic, and the liquid metal is a Newtonian laminar liquid that cannot be compressed.
2. The vaporization of the metal is not considered, when the temperature of the solid metal exceeds the melting point, it is completely transformed into molten material after the latent heat of fusion is absorbed.
3. Similar to Chu et al. [10], in this simulation, the radius of a discharge plasma channel remains constant during the whole pulse duration time.
4. The discharge maintaining voltage and discharge current remain constant during the entire pulse duration time.
5. The influence of side flushing is not considered.

4.2 Geometric modeling

According to the cross-section profiles of craters measured in Sect. 3, a simplified geometric model which schematically represents the multi-pulse discharge experiments carried out in fast ED-milling can be developed, as shown in Fig. 17a. For the sake of simplifying the calculation, a 2D axially symmetrical structure as shown in Fig. 17b is adopted in the thermal-fluid coupling model. Dominant parameters, such as gap width, machining depth, etc., are measured in actual machining, as listed in Table 3.

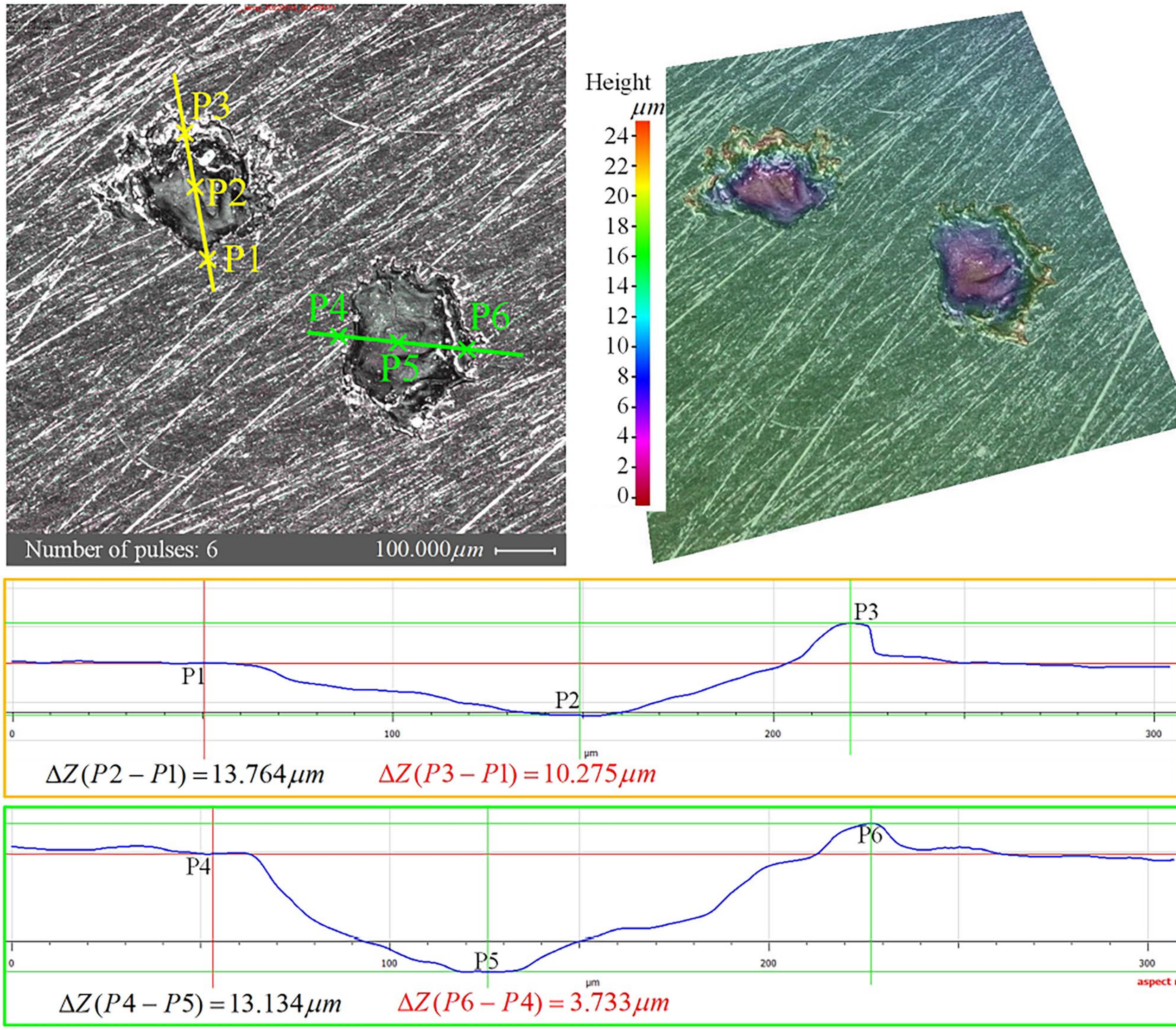

Fig. 13 Geometrical morphology of a combined crater when inner flushing is applied

4.3 Heat flux

In terms of the mechanism of material removal, fast ED-milling is in line with other EDM processes. During a discharge process, heat flux is generated by a discharge plasma channel and transferred from the surface of a workpiece to the gap and the body of the workpiece [18]. As noted by Descoeudres et al. [19] and Kojima [20], the heat flux in a discharge plasma channel obeys a Gaussian distribution. Moreover, it has been proven that as compared to a volume heat source, a surface heat source can better explain the phenomenon occurring during a discharge, and the diameter of a heat source is the same as that of a plasma channel [21]. Therefore, based on the assumptions made in Sect. 4.1, a Gaussian surface heat source adopted in the coupling model is described as

$$Q(r) = \frac{4.57P}{\pi R^2} \exp(-\frac{4.5(r - r_0)^2}{R^2}) \tag{3}$$

where r represents the coordinate of a point under the cylindrical-coordinate system (m), r_0 denotes the coordinate of a plasma channel center, R is the radius of the plasma channel (m), under the conditions used in this paper. R is found to be about 50 μm. P denotes the discharge power (W), which can be calculated by the product of the discharge maintaining voltage (18 V) and the discharge current (10 A).

To simulate the pulse duration and pulse interval, a piecewise function is utilized to control the action time of the heat flux, as described in

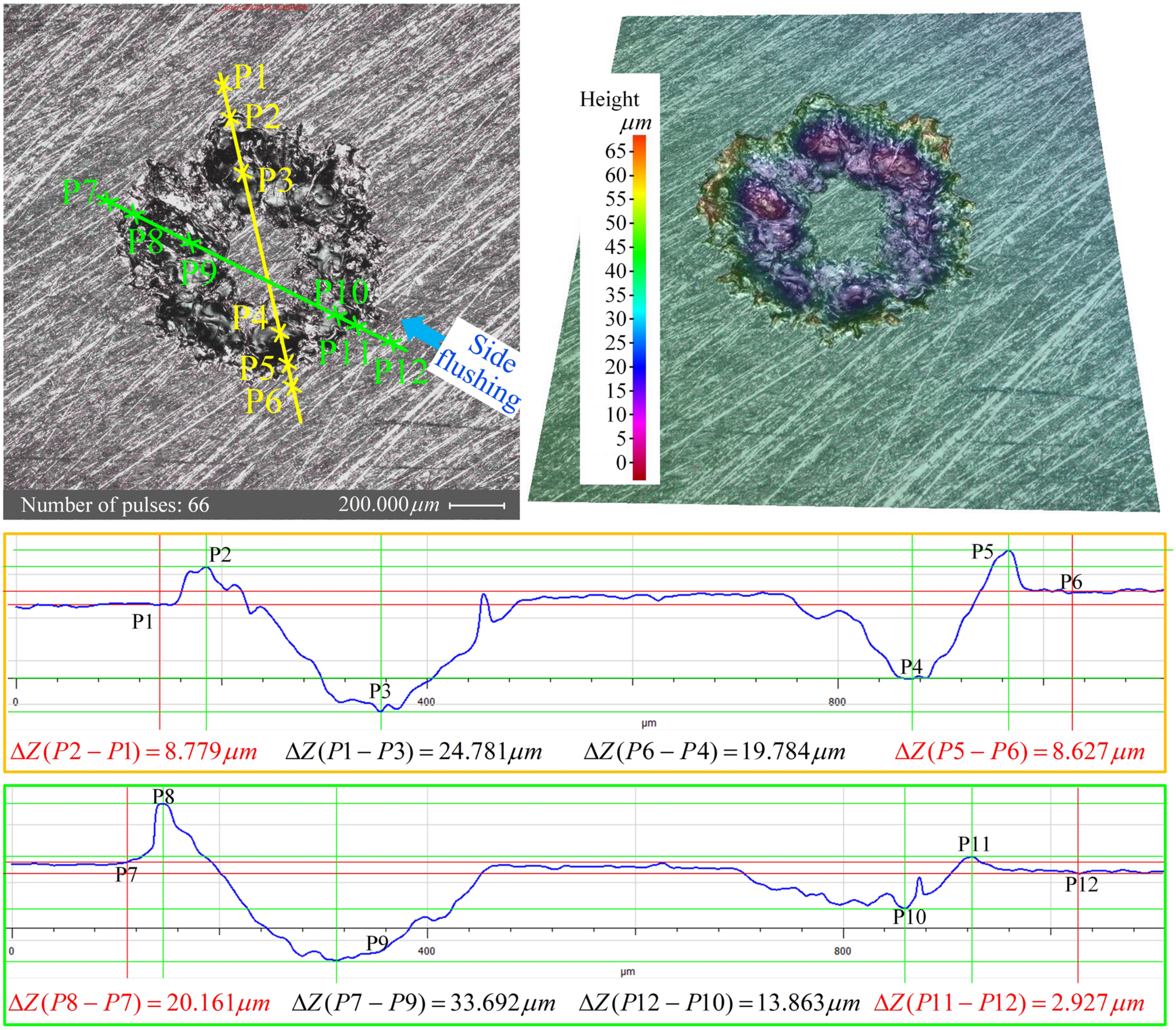

Fig. 14 Geometrical morphology of a combined crater when side and inner flushing is applied

$$h(t) = \begin{cases} 1 & 0 < t \le T_{on} \\ 0 & T_{on} < t \le T_{on} + T_{off} \end{cases} \tag{4}$$

In a pulse discharge process, the generated discharge energy is distributed among the anode, cathode, and gap. According to Xia et al. [22], when a negative tool polarity is adopted, the energy is distributed with an approximate ratio of 1:1.4:1 among the tool electrode, workpiece, and gap. Therefore, the heat flux exposed on the workpiece can be expressed as

$$Q_w(r,t) = \frac{338.94}{\pi R^2}\exp\left(-\frac{4.5(r-r_0)^2}{R^2}\right)h(t) \tag{5}$$

A boundary heat source in the heat transfer in solids and fluids module is applied to implement the heat flux. During a discharge pulse duration, the solid workpiece is continuously heated. When the temperature exceeds the melting point, the heated part is completely transformed from solid superalloy to molten metal. To determine the melting boundary of the workpiece, a phase change module is also applied. Thermophysical properties of nickel-based superalloys are listed in Table 4.

4.4 Molten material tracking

To simulate a movement process of the generated molten material under the effect of a flushing fluid, the type of a flow pattern when flowing through the gap channel needs to be determined first as laminar or turbulent. The type of flow pattern can be determined with the value of the Reynolds number as

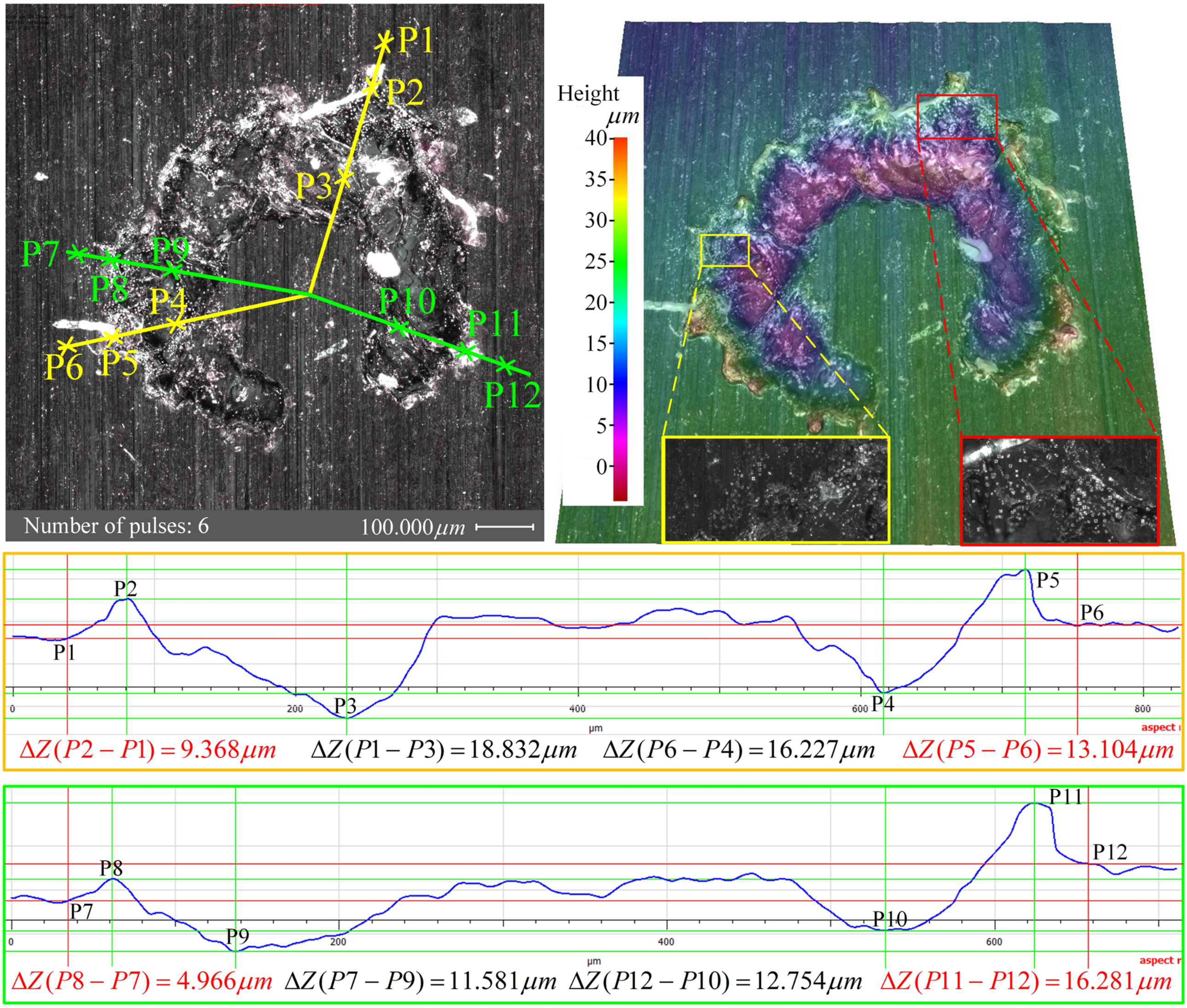

Fig. 15 Geometrical morphology of a combined crater when immersed and inner flushing is applied

$$\mathrm{Re} = \frac{\rho v d}{\mu} \tag{6}$$

where ρ (kg/m^3),v (m/s), and μ (Pa·s) represent the density, velocity, and viscosity coefficient of the fluid, respectively, and d (m) denotes the gap width. Under a flushing pressure of 0.48 Mpa, the average flow velocity is measured to be about 25 m/s, and the corresponding Reynolds number is about 4950. Therefore, in this paper, a Reynolds-averaged Navier–Stokes (RANS) model is adopted to simulate the flow field within a discharge gap and the dynamics of the turbulence are described by a standard two-equation k-ε model with realizability constraints.

To track the movement of molten material, a level-set method [24] is used. The basic idea of this method is to track moving interfaces in a fluid-flow model by solving a transport equation for the level set function $\phi(p,t)$. In the coupling model developed in this paper, $\phi(p,t)$ is defined as

$$\phi(p,t)\begin{cases} 1\ r \in \textit{flushing liquid} \\ 0\ r \in \textit{molten material} \end{cases} \tag{7}$$

where p denotes the position coordinate (m), and t represents the time (s). To update $\phi(p,t)$ by calculating the velocity field of molten material, the transport equation can be written as

$$\frac{\partial \phi}{\partial t} + \mathbf{u}\cdot\nabla\phi = \gamma\nabla\cdot\left(\varepsilon_{ls}\nabla\phi - \phi(1-\phi)\frac{\nabla\phi}{|\nabla\phi|}\right) \tag{8}$$

where ϕ is the level-set function introduced above, $\mathbf{u}$ denotes the moving speed of the molten material (m/s), γ is the

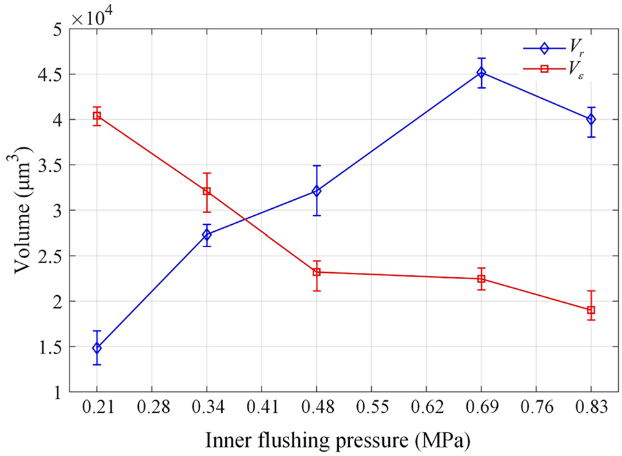

Fig. 16 Effects of inner flushing pressure on V_r and V_ε

reinitialization speed (m/s), and ε_{ls} is the parameter controlling interface thickness.

4.5 Governing equations

In the developed thermal-fluid coupling model, heat transfer in solids and fluids, turbulent two-phase flow with a level set method, and phase change are comprehensively considered. To achieve a combined solution of the temperature, flow, and velocity field, the RANS equation for conservation of momentum, the continuity equation for conservation of mass, and the heat transfer equation, as described in Eq. (9) through Eq. (11), need to be simultaneously satisfied.

$$\rho\frac{\partial \mathbf{u}}{\partial t}+\rho(\mathbf{u}\cdot\nabla)\mathbf{u}=\nabla\cdot\left[-p\mathbf{I}+\mu(\nabla\mathbf{u}+(\nabla\mathbf{u})^T\right]+\mathbf{F} \tag{9}$$

$$\rho\nabla\cdot(\mathbf{u})=0 \tag{10}$$

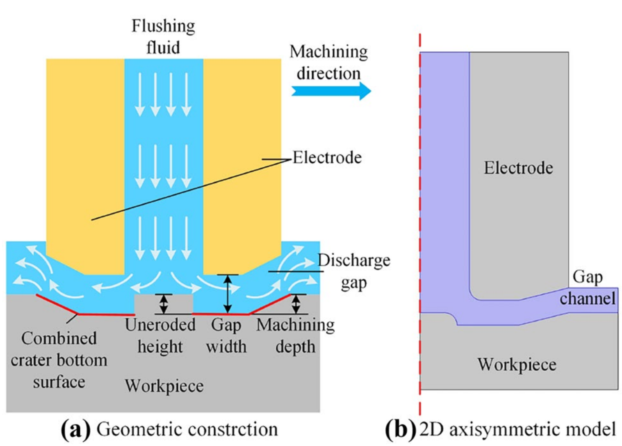

Fig. 17 Geometric construction of fast ED-milling and its corresponding 2D axisymmetric structure

Table 3 The geometric dimension of the axisymmetric model

Parameter	Electrode outer diameter	Electrode inner diameter	Gap width	Machining depth	Uneroded height
Value (mm)	0.6	0.2	0.05	0.025	0.025

$$\rho C_P\frac{\partial T}{\partial t}+\rho C_P\mathbf{u}\cdot\nabla T=k\nabla\cdot\nabla T+Q \tag{11}$$

where ρ is density (kg/m^3), t is time (s), $\mathbf{u}$ denotes the velocity field (m/s), p is the pressure (Pa), $\mathbf{I}$ is the identity matrix,μ is dynamic viscosity (Pa·s), $(\nabla\mathbf{u})^T$ represents the transposed matrix of $\nabla\mathbf{u}$, $\mathbf{F}$ denotes the volume force, C_P heat capacity at constant pressure (J/kg/K), T is the absolute temperature (K), k denotes thermal conductivity (W/m/K), and Q is the heat source (W/m).

4.6 Boundary conditions

Boundary conditions for the thermal-fluid coupling model are schematically illustrated in Fig. 18. The computational domain of this model consists of three parts, namely the electrode (brass), gap channel (water), and workpiece (nickel-based superalloy). As for the thermal boundary conditions, boundaries in the model are classified into four categories and each category is shaded with different colors enclosed with solid lines. As shown in Fig. 18, a purple line represents a heat flux across boundary, a black line represents a thermal insulation boundary, a red line represents a heat conduction boundary, and a blue line represents a heat convection boundary. A heat conduction boundary where the boundary heat source is applied can be defined as

$$k\mathbf{n}\cdot\nabla T=Q_w(r,t) \tag{12}$$

A thermal insulation boundary is defined by Eq. (13). A heat convention boundary and a heat flux across boundary are defined by the same Eq. (14) with different heat transfer coefficients.

$$k\mathbf{n}\cdot\nabla T=0 \tag{13}$$

Table 4 Thermophysical properties of nickel-based superalloys

Property (unit)	Value
Density (kg/m^3)	8180
Melting point (K)	1798
Thermal conductivity (W/m/K)	11.5
Heat capacity at constant pressure (J/kg/K)	446
Latent heat of fusion (J/kg)	3.33×10^5
Dynamic viscosity of liquid phase (Pa·s)	0.001 [23]
Ratio of specific heats	1

$$k\mathbf{n}\cdot\nabla T = h_c(T - T_0) \tag{14}$$

where h_c denotes the heat transfer coefficient (W/m^2/K), T_0 is the ambient temperature (293.15 K), $\mathbf{n}$ represents the normal direction to the boundary, and other parameters are the same as described in Sect. 4.5.

With regard to the fluid boundary conditions, as demonstrated in Fig. 18, the inlet and outlet of a flushing fluid can be respectively defined as

$$\mathbf{n}^T\left[-p\mathbf{I}+\mu(\nabla\mathbf{u}+(\nabla\mathbf{u})^T\right]\mathbf{n} = -p_0^{in} \tag{15}$$

$$\left[-p\mathbf{I}+\mu(\nabla\mathbf{u}+(\nabla\mathbf{u})^T\right]\mathbf{n} = -p_0^{out}\mathbf{n} \tag{16}$$

where $\mathbf{n}^T$ is the transpose of a boundary normal vector $\mathbf{n}$ pointing out of the domain, p_0^{in} is the flushing pressure (0.48 MPa), and p_0^{out} represents the ambient pressure (1 atm). The remaining boundaries of the flow field except for the symmetrical axis are defined as walls (depicted with blue lines), which can be formulated by

$$\mathbf{u} = \mathbf{0} \tag{17}$$

5 Simulation results and analysis

With the coupling model, in this section, the dynamic evolution process of molten material, and the velocity, pressure, and temperature distributions inside the discharge channel are investigated. Under the parameters listed in Table 2, a single pulse discharge process is simulated by the model, so that the complete process of generation, movement, and solidification of molten material under

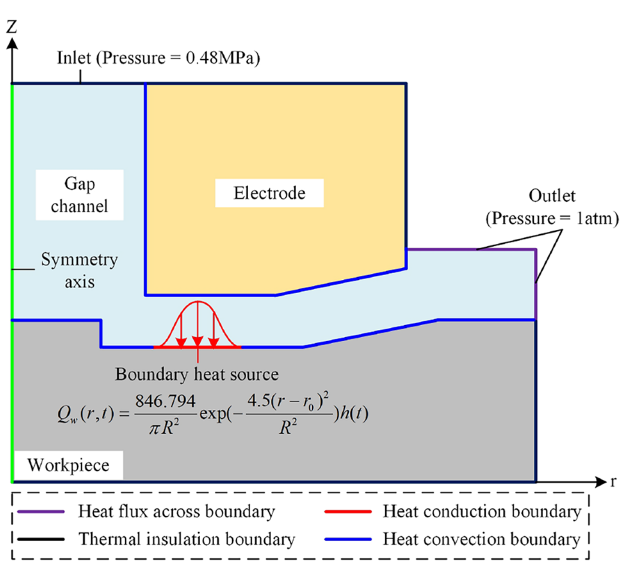

Fig. 18 Boundary conditions of the thermal-fluid coupling model

the effect of high-pressure inner flushing can be better understood. A time-dependent study with a parallel sparse direct solver (PARDISO) is applied to solve the governing functions given in Sect. 4.6, and the results are as follows.

5.1 Analysis of the molten material

Under the continuous action of the Gaussian surface heat source, the solid workpiece material around the discharge position is gradually melted to form the molten material. To simulate the evolution process of the molten material, a phase change module is also applied in the coupling model. With the help of a phase indicator, the generation, movement, and solidification process of the molten material can be visualized.

It is worth mentioning that this simulation aims to investigate the morphology of the combined crater, the molten material produced by a single discharge will affect the combined crater morphology only when it is thrown into the discharge gap. Therefore, this simulation only focuses on the moving trend of expelled molten material located on the bottom surface of the combined crater under the action of a flow field. As for the evolution and expelling process of molten material in a molten pool, it belongs to the research category of the dimension of a single discharge crater and rarely has effect on the combined crater morphology.

Figures 19 and 20 illustrate the evolution process of the molten material when the discharge occurs at the front and lateral surface of the electrode, respectively. From the figures, it can be seen that the molten material starts to produce in the gap channel at 1 μs after the beginning of a discharge. During the whole pulse duration, new molten material is continuously generated, resulting in a gradual increase in the radius of a molten region. However, the generated molten material is asymmetric with respect to the center of the plasma channel. This phenomenon, which is of great discrepancy with a traditional EDM, is because of the following reasons. For one thing, the high-pressure flushing fluid impedes the expansion of the plasma channel towards the electrode center, which causes a difference in the expansion velocities of the molten pool along the left and right directions of the plasma channel center. For the other, the generated molten material moves along the workpiece surface towards the outlet of the discharge gap under the action of the fluid force, which leads to an increase in the molten material size on the right side of the plasma channel center. The combined action of these two factors leads to an asymmetric growth of the molten pool, which can be confirmed in Figs. 19 and 20. With the entering of a pulse interval, the radial size of the molten pool decreases sharply and finally disappears at 16 μs or 17 μs.

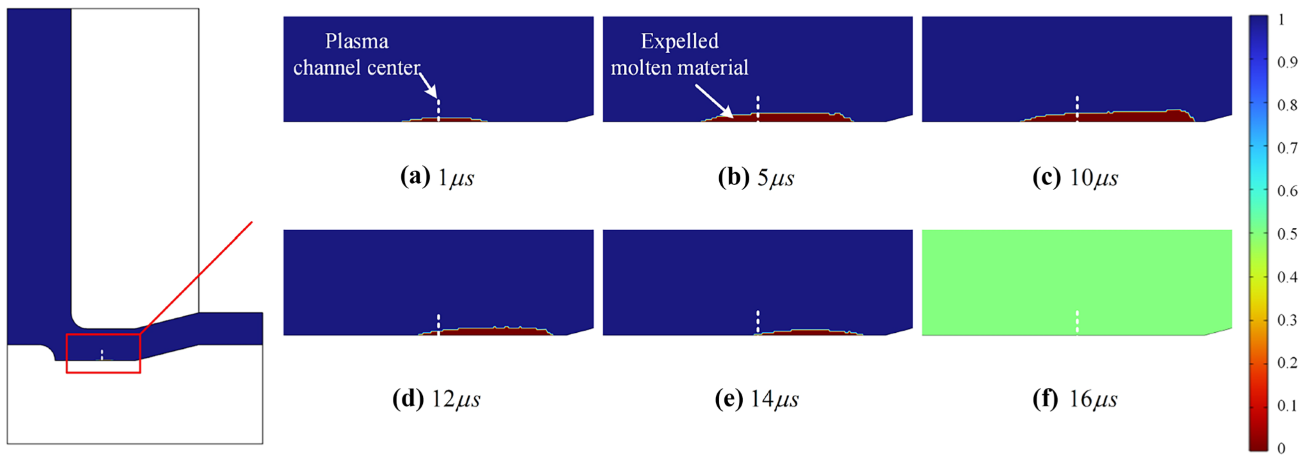

Fig. 19 Evolution process of the molten material within the simulation period when the discharge occurs at the front surface of the electrode

In terms of the molten material movement, traditional EDM and fast ED-milling are different. While in traditional EDM methods, molten material detaches from a molten pool in a splashing way [16], in fast ED-milling, the expelled molten material moves along the workpiece surface under the action of a flow field. Under the strengthened cooling of a flushing fluid, the molten material gradually solidifies while moving, resulting in the cumulation of molten material around the outside of a single pulse discharge crater. Due to the sequential occurrence of discharges during a multi-pulse discharge experiment, the molten material will eventually accumulate around the outside of the combined crater that is near the external surface of the electrode. Recalling Fig. 13 through Fig. 15 in Sect. 3.2, it can be concluded that the simulation results provide a good explanation of the mechanism for the directionality of craters occurring during experiments for investigating flushing conditions.

5.2 Analysis of the velocity field

The velocity distribution in the gap channel as an evolution is illustrated in Fig. 21. Under an inlet pressure of 0.48 MPa, the maximum velocity of a flushing dielectric fluid can reach as high as 35 m/s. For high-speed EDM drilling, the maximum velocity of the gap channel is located at the first corner of an electrode [10]. By contrast, for fast ED-milling, the maximum velocity appears near the discharge position, which means that the velocity of the flushing fluid is increased after entering the gap channel. This is because the gap channel of a fast ED-milling does not have continuous corners like that of a high-speed EDM drilling. After entering the gap channel, the velocity of the flushing fluid can be significantly increased since the gap width was much smaller than the inner diameter of the electrode. The hydrodynamic force F_v induced by such a flushing velocity drives

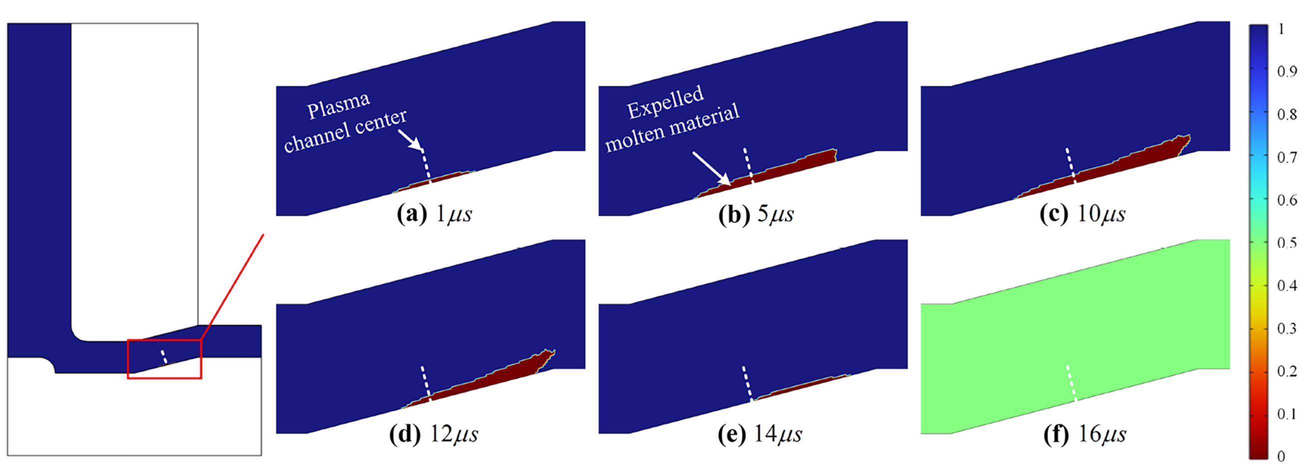

Fig. 20 Evolution process of the molten material within the simulation period when the discharge occurs at the lateral surface of the electrode

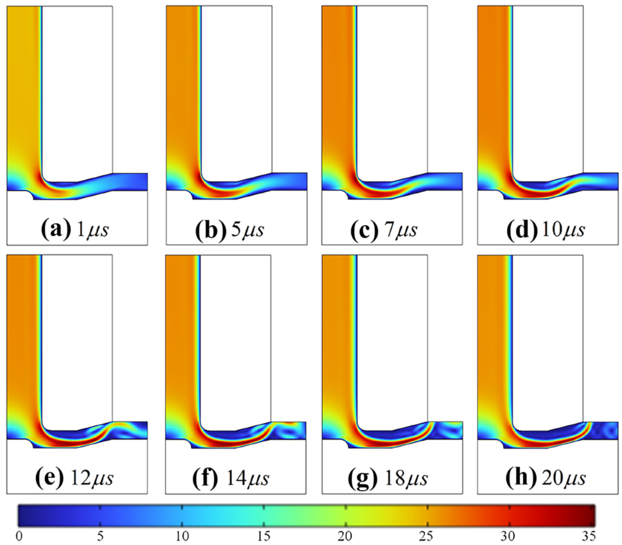

Fig. 21 Velocity distribution in the discharge gap within the simulation period

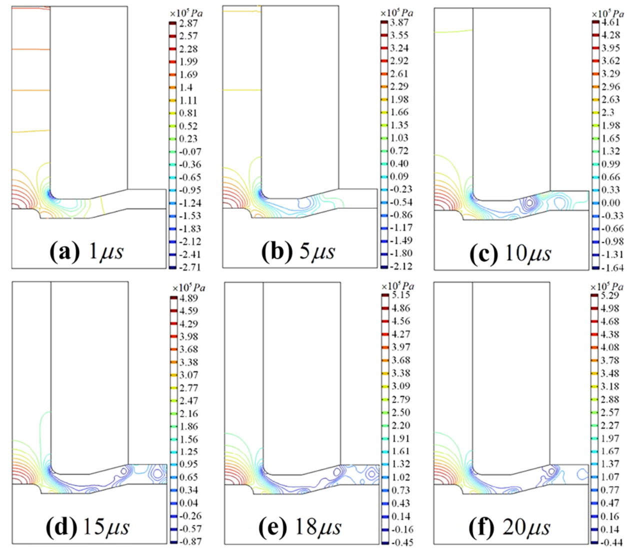

Fig. 22 Pressure distribution in the discharge gap within the simulation period

the molten material moving along the workpiece towards the outlet of the gap channel. As a result, large bulges are formed near the external surface of the electrode. The direction of the hydrodynamic force F_v is consistent with the flushing dielectric fluid and can be calculated by Eq. (18), where ρ, $\mathbf{u}$ denote the density and velocity of the flushing dielectric fluid, S is the lateral area of the molten material facing the flushing direction. Moreover, the velocity of the flushing fluid near the electrode tip is approximately zero. Unlike craters on the workpiece surface, craters on the electrode tip will not have noticeable directionality. This simulation provides a reasonable explanation for the cross-section profile measured in Sect. 3.2.

$$F_v = \rho \cdot S \cdot \mathbf{u}^2 \tag{18}$$

5.3 Analysis of the pressure field

In fast ED-milling, the distribution of pressures in a discharge gap channel is significantly affected by a high-pressure flushing dielectric fluid. Figure 22 illustrates the pressure field in the discharge gap at different simulation moments with an inlet flushing pressure of 0.48 MPa. From the figure, it can be seen that the highest and the lowest points of pressure are located at the surface of the uneroded part and the internal corner of the electrode, respectively. The pressure difference between the uneroded part surface and the discharge spot reaches as high as 0.58 MPa, which is far beyond that of the atmospheric pressure. Such a large pressure difference determines the moving direction of the generated molten material, which is the reason why the molten material is mainly accumulated on the side of a crater that deviates from the center of the electrode. Moreover, the pressure difference also prevents an expansion of the plasma channel towards the electrode center, which is the reason for an asymmetric growth of the molten pool as shown in Fig. 19. Referring to the crater morphology measured in Sect. 3.2, it can thus be concluded that the simulation results get a satisfactory agreement with the experimental observations.

5.4 Analysis of the temperature field

By a temperature field analysis, the heating and cooling processes of a workpiece, the heat convection between the molten material and the flushing dielectric liquid, and the heat conduction between the molten material and the workpiece can be visualized. As shown in Fig. 23, the temperature near the discharge spot begins to exceed the melting point of the workpiece at 1 μs after the beginning of a discharge. This means that the molten material begins to be generated at this moment. Under the effect of heat conduction, the heat generated by the discharge transfers to the un-melted region of the workpiece, which results in an expansion of the molten pool along both the radial and depth directions. The expansion speeds in these two directions are different due to the effect of the flushing fluid. As the single discharge process proceeds, the maximum temperature of the molten pool continuously increases, and at the end of the discharge, the maximum temperature of the molten pool is decreased. This can be explained by the fact that during a period of 1 μs, the heat taken away by both the expelled molten material and the flushing fluid is larger than the heat generated by a

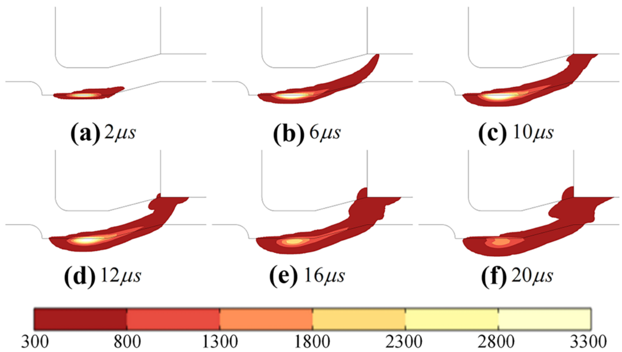

Fig. 23 Temperature distribution of the gap channel within the simulation period

discharge, resulting in a net heat loss of the molten pool. With the entering of a pulse interval, under the strengthened cooling effect of high-speed flushing, the temperature of the molten pool decreases rapidly. The position with the maximum temperature has gradually moved from the surface of the molten pool to the inside of the workpiece. At 16 μs, the temperature of the molten pool surface has dropped below the melting point of 1798 K. Although the temperature inside the molten pool is still greater than the melting point, the flushing fluid at this time will not be able to act on the newly generated material, and the geometric morphology of the discharge crater will remain approximately unchanged. After the end of the pulse interval, the temperature of the workpiece has not been cooled to its initial value, but new molten material cannot be generated.

Another noticeable finding in this figure is that the flushing fluid also consumes a part of the heat generated by the discharge while promoting the evacuation of the molten material. Referring to the experimental results illustrated in Fig. 16, as the flushing pressure increases, the absolute material removal volume increases first and then decreases. This phenomenon can be attributed to the increasing heat consumption of the fluid. To confirm this conjecture, the maximum temperature of the molten pool at different simulation moments under various flushing pressure is investigated by the coupling model and the results are demonstrated in Fig. 24.

In Fig. 24, solid or dash lines are, respectively, used to indicate whether the maximum temperature of the molten pool at a certain moment is higher or lower than the melting point of the workpiece material. In other words, a solid line represents a period in which new molten material can be generated, a dash line represents a period in which new molten material cannot be generated. From the figure, it can be seen that as the flushing pressure increases, both the maximum temperature of the molten pool at the end of a discharging and the total time period when the maximum temperature exceeds the material's melting point decreases significantly. This means that when the flushing pressure is inappropriately high, the heat consumed by heat convection will account for a dominant part of the total heat. As a result, the generation of molten material is insufficient. The insufficient generation of molten material will directly lead to a decrease in the absolute material removal volume per discharge, which is the mechanism of the unexpected decline that occurred in the experiment performed in Sect. 3.3.

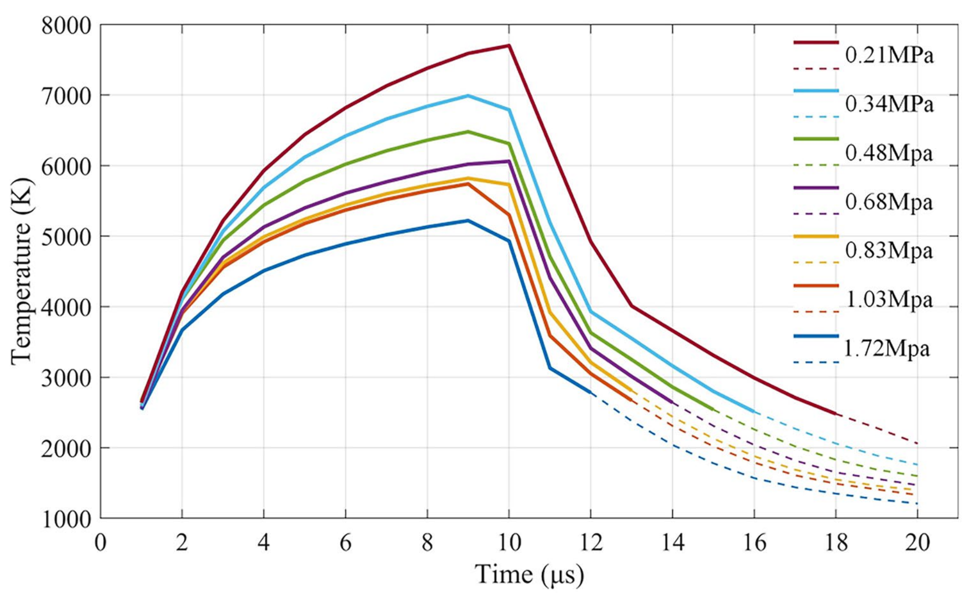

Fig. 24 Maximum temperature of the molten pool at different simulation moments under various flushing pressure

6 Conclusions

This study achieves a better understanding of the machining mechanism of the fast ED-milling process and provides some hints for process optimization. The following conclusions can be drawn:

(a) Under an immersed flushing, the use of deionized water cannot obtain a better machining performance than EDM-oil.
(b) The use of high-pressure inner flushing is the main reason why fast ED-milling has a higher machining efficiency than conventional ED-milling.
(c) A combination of side and inner flushing is the best flushing condition for fast ED-milling.
(d) In fast ED-milling, the molten material moves along the workpiece surface towards the outlet of the gap channel under the action of a flow field.
(e) The inner flushing pressure must be appropriately chosen for a high machining efficiency. When the inner flushing pressure is inappropriately high, the severe heat consumption caused by heat convection will lead to a decrease in the absolute material removal volume per discharge.

In summary, this study gains further insight into the mechanism of the efficient removal of material of a promising machining technology, which can contribute to the knowledge and increase EDM implementation rate. Besides, the fast ED-milling method can be of interest to the manufacturing industry for film cooling holes of turbine blades. Moreover, the research methodology introduced in this paper can also be applied to mechanism investigation in other EDM processes.

Acknowledgements The authors thank Dr. Xiao-Lei Yu, who provided valuable feedback on early drafts of this work.

Author contribution Jian Wang: methodology, conceptualization, software, validation, formal analysis, writing — original draft and editing. Xue-Cheng Xi: funding acquisition, supervision, reviewing and editing. Hao-Yu Chu: formal analysis, software, validation. Ya-Ou Zhang: formal analysis, validation. Fu-Chun Zhao: validation. Wan-Sheng Zhao: funding acquisition, supervision, reviewing and editing.

Funding This work is financially supported by the National Natural Science Foundation of China (No. 52075333, 52175426), and the National Science and Technology Major Projects of China (No. 2018ZX04005001).

Availability of data and materials The datasets used or analyzed during the current study are available from the corresponding author on reasonable request.

Code availability This paper uses a proprietary software and will be not available.

Declarations

Ethics approval and consent to participate Not applicable.

Consent for publication Not applicable.

Competing interests The authors declare no competing interests.

References

1. Yu Z, Masuzawa T, Fujino M (1998) Micro-EDM for three-dimensional cavities-development of uniform wear method. CIRP Ann 47(1):169–172
2. Bellotti M, Caballero JRDE, Qian J, Reynaerts D (2021) Effects of partial tool engagement in micro-EDM milling and adaptive tool wear compensation strategy for efficient milling of inclined surfaces. J Mater Process Technol 288:116852
3. Pei J, Liu Y, Zhu Y, Zhang L, Zhuang X, Wu S (2018) Machining strategy and key problems for 3D structure of micro-EDM by fix-length compensation method with tubular electrodes. Procedia CIRP 68:802–807
4. Huang H, Bai J-C, Lu Z-S, Guo Y-F (2009) Electrode wear prediction in milling electrical discharge machining based on radial basis function neural network. J Shanghai Jiaotong Univ (Science) 14(6):736–741
5. Kliuev M, Boccadoro M, Perez R, Dal Bó W, Stirnimann J, Kuster F, Wegener K (2016) EDM drilling and shaping of cooling holes in Inconel 718 turbine blades. Procedia CIRP 42:322–327
6. Kliuev M, Wegener K (2020) Method of machining diffusors in Inconel 718 turbine blades for film cooling using EDM drilling and shaping. Procedia CIRP 95:511–515
7. Kliuev M, Kutin A, Wegener K (2021) Electrode wear pattern during EDM milling of Inconel 718. Int J Adv Manuf Technol 117(7):2369–2375
8. Xia W, Zhang Y, Chen M, Zhao W (2020) Study on gap phenomena before and after the breakout event of fast electrical discharge machining drilling. J Manuf Sci Eng-Trans ASME 142(4):041004
9. Zhang Y, Liu Y, Shen Y, Ji R, Li Z, Zheng C (2014) Investigation on the influence of the dielectrics on the material removal characteristics of EDM. J Mater Process Technol 214(5):1052–1061
10. Chu H, Xi X, Li Z, Zhang Y, Zhao W (2021) Study on the evolution process of recast layer for fast EDM drilling based on observation experiment and a novel thermal-fluid coupling model. J Phys D Appl Phys 54(32):325501
11. Zhu Y, Gu L, Farhadi A, He G, Zhao W (2019) Observation and analyzation of plasma channel evolution behavior in air flushing electrical arc machining. Int J Adv Manuf Technol 100(9):3127–3138
12. Yue X, Yang X, Li Q, Li X (2020) Novel methods for high-speed observation of material removal and molten pool movement in EDM. Prec Eng 66:295–305
13. Zhang F, Gu L, Chen J, Xu H, Zhao W (2016) Observation and modeling research of high-velocity flushing effect on the performance of BEAM. Int J Adv Manuf Technol 86(1):935–942
14. Natsu W, Ojima S, Kobayashi T, Kunieda M (2004) Temperature distribution measurement in EDM arc plasma using spectroscopy. JSME Int J Ser C 47(1):384–390
15. Kitamura T, Kunieda M, Abe K (2015) Observation of relationship between bubbles and discharge locations in EDM using transparent electrodes. Prec Eng 40:26–32
16. Tang J, Yang X (2017) A novel thermo-hydraulic coupling model to investigate the crater formation in electrical discharge machining. J Phys D Appl Phys 50(36):365301

17. Tang J, Yang X (2018) Simulation investigation of thermal phase transformation and residual stress in single pulse EDM of Ti–6Al–4V. J Phys D Appl Phys 51(13):135308
18. Li Z, Bai J, Tang J (2018) Experimental investigation on the discharge stability in micro-EDM based on finite-successive pulses discharge method. J Phys D Appl Phys 51(47):475104
19. Descoeudres A, Hollenstein C, Wälder G, Perez R (2005) Time-resolved imaging and spatially-resolved spectroscopy of electrical discharge machining plasma. J Phys D Appl Phys 38(22):4066
20. Kojima A (2007) Observation of arc plasma expansion and delayed growth of discharge crater in EDM. Proc ISEM 1–4
21. Kojima A, Natsu W, Kunieda M (2008) Spectroscopic measurement of arc plasma diameter in EDM. CIRP Ann 57(1):203–207
22. Xia H, Kunieda M, Nishiwaki N (1996) Removal amount difference between anode and cathode in EDM process. Ijem 1:45–52
23. Quested PN, Brooks RF, Chapman L, Morrell R, Youssef Y, Mills KC (2009) Measurement and estimation of thermophysical properties of nickel based superalloys. Mater Sci Technol 25(2):154–162
24. Osher S, Sethian JA (1988) Fronts propagating with curvature-dependent speed: algorithms based on Hamilton-Jacobi formulations. J Comput Phys 79(1):12–49